Heliyon 10 (2024) e40899

Contents lists available at ScienceDirect

Heliyon

journal homepage: www.cell.com/heliyon

Research article

# Experimental and numerical investigation of dissimilar weld characterization in laser welding of duplex 2205 and AISI 1060 steel: Microstructure, mechanical properties and weld geometry

Mohammad Behzad Botlani Esfahani [a], Arash Karimipour [a,b,*], Mohammad Akbari [a,b], Ali Abdollahi [c,d], Mohammad Najafi [c]

[a] Department of Mechanical Engineering, Najafabad Branch, Islamic Azad University, Najafabad, Iran
[b] Aerospace and Energy Conversion Research Center, Najafabad Branch, Islamic Azad University, Najafabad, Iran
[c] Department of Mechanics, Electrical Power and Computer, Science and Research Branch, Islamic Azad University, Tehran, Iran
[d] Modern Automotive Research Center, Science and Research Branch, Islamic Azad University, Tehran, Iran

ARTICLE INFO

*Keywords:*
Dissimilar laser welding
AISI 1060 carbon steel
Duplex stainless steel 2205
Weld characterizations
Response surface methodology (RSM)
Microstructural changes

ABSTRACT

Dissimilar laser welding of martensitic AISI 1060 carbon steel and Duplex Stainless Steel 2205 was performed based on an experimental and numerical study. The experiments were then conducted based on central composite design experiments (CCD) and analyzed via the response surface methodology (RSM) by considering the effect of laser welding process parameters (incident laser power, speed of welding, nozzle distance and deviation of laser beam) on the weld joint characterization. The experimental results showed that the laser power had a remarkable effect on the melt pool depth. By increasing the laser power from 250 to 450 W at the focal point position, the melt pool depth was increased from 0.4 to 1.4 mm. The microstructure of the molten pool was mainly composed of the solidification of duplex stainless steel (DSS). The molten pool microstructure included columnar dendritic and inter-dendritic microstructures at the boundary fusion line of the toward duplex 2205 base metal. The cellular microstructure with epitaxial grain growth at the center of the molten pool was then formed. According to the numerical simulation results, by increasing the laser power from 250 to 400 W, the extension of high temperature region (more than 1800 °C) was raised to about 150 percent at both depth and width. According to the tensile tests results, the joint fracture surface of the carbon steel side of the joint showed a brittle fracture mechanism due to the martensitic nature of the microstructure of carbon steel, while the fracture cross-section of the DSS side of the joint had a mostly ductile fracture mode, as compared to carbon steel. By increasing the laser beam energy density to more than 0.05 MW/cm2, a coarse grain cellular dendrite was formed at the fusion zone toward AISI 1060 steel along with tempered martensitic microstructure at the heat affected zone of the AISI1060 base metal. This led to the transformation of the joint fracture mechanism from a brittle one to a ductile one. The maximum tensile stress of the dissimilar joints was lower than that of both base metals, although the maximum tensile strength of 550 MPa was obtained at the focal point position and the laser power of 450 W. By increasing the laser power from 400 to 450 W, the microhardness at the region near the fusion line of the duplex stainless steel was increased by about 50 HV, while at the center of the fusion zone, the maximum increase rate reached to 250 HV.

* Corresponding author. Department of Mechanical Engineering, Najafabad Branch, Islamic Azad University, Najafabad, Iran.
*E-mail address:* arashkarimipour@gmail.com (A. Karimipour).

https://doi.org/10.1016/j.heliyon.2024.e40899
Received 26 July 2024; Received in revised form 15 November 2024; Accepted 2 December 2024
Available online 4 December 2024

## 1. Introduction

Different methods have been utilized for joining dissimilar metals including steel to copper base alloys, steel to aluminum, stainless steel to nickel base alloys, etc. Friction welding, the high-frequency resistance process, diffusion welding, percussion welding and electron beam welding are common methods of joining dissimilar materials. Every method has its own advantages including high speed for high frequency resistance welding widely used for dissimilar welding of copper to steel metal. The Friction welding has a very small heat-affected zone, the base metal heated region and therefore, the intermetallic material formation with wide application for joining dissimilar joining of steel to copper base alloys, steel to aluminum, stainless steel to nickel base alloys. The electron beam welding process is known as the methods with wide application for joining dissimilar metals at fast welding speed. It can overcome the different thermal conductivity of material with extremely small weld zone. The small amount of intermetallic compound formed in electron beam welding does offer an advantage for many dissimilar combinations. Apart from mentioned methods, the gas tungsten and the gas metal arc welding processes have had wide application on joining dissimilar metals. Dissimilar welding can provide the advantage of each material's superior properties to produce a joint with higher quality to improve the unique joints productively [1–4]. Such a dissimilar joint with different stainless steel grades can be combined with other materials; this joint is widely used in oil refineries, petrochemical industries, energy production and power plants industries [5]. Laser welding of DSS 2205 with other materials has been utilized in different industries due to having superior mechanical properties, as compared to commercial austenitic stainless steel grades [6,7]. High corrosion resistance and excellent mechanical properties have boosted the usage of these materials in various industries such as petrochemical, oil and gas, and the military. The microstructure of DSS has an equal network of austenite and ferrite, which balances the material properties. By examining the microstructure of the material after laser welding, it is possible to effectively evaluate the changes of the materials' properties at the welding line [8–11]. The welding process of DSS by different methods and its various applications shows the enormous potential of this material in different industries [12–14].

Dissimilar welding of DSS with other materials has been investigated in numerous studies to assess the characterization of new dissimilar joints. In this regard, Khan and Chhibber [15] investigated the microstructure and mechanical properties of the dissimilar weld joint of super DSS 2507 and API X70 steel by using arc welding. The tensile and impact properties of the weld produced by laboratory electrodes had considerable ductility and impact energy, as compared to the commercial electrode.

Ceyhun et al. [16] also investigated the laser welding of super-duplex AISI 2507 and super-austenitic 904L stainless steel sheets at different laser powers and speeds. At the low heat input, an increase in tensile strength, yield strength and hardness was observed, as compared to the samples welded with the high heat input. By using heat treatment, a decrease in elasticity, yield strength and hardness, and an increase in ductility and toughness were observed. Abdo, H.S et al. [17] also evaluated the corrosion resistance and microstructure modification properties of DSS 2205 by adjusting the welding parameters of the pulsed Nd: YAG laser beam. They found that welding with high pulse energy resulted in higher corrosion resistance. Saravanan et al. [18] also analyzed the effect of welding parameters on the joint's mechanical properties and microstructure of DSS. They reported that at the higher heat input, more porosities were formed at the fusion zone. The maximum tensile and yield strength was obtained for test conditions with the lower input heat. Laser dissimilar welding of A516 pressure vessel carbon steel and DSS 2205 was also investigated by Karimi et al. [19]. They found that the ultimate tensile stress of the welded joint equal to 500 MPa occurred at the focal point position, where the laser beam irradiated the workpiece surface, with the speed of 300 mm/min and power of 400 W. According to the results, the incident power of the beam to the workpiece surface and the speed of movement had the greatest effect on the weld joint's tensile properties. Examination of the weight percentage elements for welding surface also showed that the nickel and chromium in the welding line had a great impact on the joint mechanical properties. Further, Moradi et al. [20] investigated the microstructural changes of the fusion zone of DSS 2304 with Inconel 718. They focused on optimizing process parameters and achieving maximum failure resistance. It was shown that the weld joint fracture force was gradually increased with the augmentation of the weld velocity and focal point position of the laser beam. The maximum breaking force was gained at the laser power of 1900 W and welding speed of 3 mm/s at the focal distance of 0 mm. The weld metal microstructure at the centerline of the melt pool was composed of concentric grains, while columnar grains were formed at the fusion line.

Laser welding of high carbon steel materials is usually known as a challenge due to creating crack and a fully martensite microstructure at the fusion zone. The high heating and severe cooling cycle induced through high carbon content of the workpiece material are the major reasons for the creation of defect, which limits the mechanical properties of the weld joint. In this study, by combining DSS and carbon steel, some new influential factors had a direct impact on the mechanism of cracks creation, the volume and percentage of martensite microstructure formation via different alloy composition mechanisms, and the temperature gradient at the fusion zone by inducing different thermal conductivity rates. By measuring the temperature during dissimilar welding according to the variation of laser welding process parameters, the resultant temperature field, microstructural variation and mechanical properties of the welded joints were evaluated, which had not been comprehensively investigated in previous studies. By using both design of experiments and numerical simulation, this study presents comprehensive results for the dissimilar welding of these materials' configuration via the analysis of temperature field, weld zone microstructure and mechanical properties of the joint. Therefore, a dissimilar joint with AISI 1060 steel and DSS 2205 configuration was performed to explore the possible relationship between the experimental data and the microstructural and mechanical characterization of the dissimilar joint, which has not been comprehensively studied before.

## 2. Laser welding experiments

### 2.1. Materials

For laser welding, two workpieces materials were prepared with the thickness of 1.5 mm and dimensions of 20 × 50 mm. The metals' chemical composition and mechanical properties for AISI 1060 steel and DSS 2205 stainless steel are shown in Table 1. A fiber laser with the output power of 1.5 KW and multi-mode beam was utilized for laser welding. The BW240 laser welding head with side blow nozzle was also applied for the welding experiments. An Argon gas bellows with the flow rate between 1 and 1.8 lit/min was also applied to protect the melt pool and adjacent regions. The 2.5 axis stepper motor CNC table was implemented for the laser beam transition at a determined path and speed. For metallography analysis, the samples were mounted and this was followed by grinding and polishing. Finally, they were etched under the ASTM E3 standard. For the microstructural analysis of the weld joint and base metals, the optical microscope, model BX53M, was utilized. Tensile test of the welded joints was performed using AL7000-MT universal tensile testing machine. The tensile tests samples were then prepared according to the ASTM E8 standard. The microhardness of the welded samples was analyzed by microhardness tester. The load of 100 g was applied at the dwell time of 10 s.

### 2.2. Experimental design

A set of experiments were designed using the central composite experimental design to assess the effect of dissimilar laser welding process parameters on the geometry of melt pool (width and depth), the temperature field at the region vicinity of the fusion zone on each material and the tensile strength of the welded joint. Four main parameters including laser power, nozzle distance from the beam focal point position, the linear laser beam speed and the amount of deviation from the contact line of the workpieces were selected as the input variables.

By conducting some initial tests shown in Table 2, the limits of the process parameters and their intervals variations were determined to evaluate and select the parameters levels and number of the main tests. Based on the preliminary experiments results, it was found that beam deviation and laser power played an important role in dissimilar laser welding characteristics of these two materials. Therefore, the parameters' level selection of the main experimental design matrix for the laser power was between 250 and 450 W; for the beam deflection, this was between −0.5 and + 0.5, the focal distance varied from −2 to 6 mm and the welding speed was selected between 200 and 300 mm/min. The experimental design was performed via the central composite design for the experiments. By considering 4 factors, usually 30 numbers of experiments, including 16 Cube points, 4 Center points in cube, 2 Center points in axial and 8 Axial points, by considering the value of alpha (2 for this design) and 5 levels (−2, −1, 0, 1 and 2), were considered for each factor to perform the CCD experimental design.

## 3. Numerical simulation

A mathematical model utilizing the finite volume method was created to examine the process of keyhole laser welding. The model is three-dimensional and time-dependent. A solidification/melting model was employed to simulate the interaction between the solid and liquid phases. A thermal model employing elliptical and cylindrical heat sources was utilized to simulate the absorption of energy from laser beam radiation. The elliptical heat source was used to model the absorbed energy on the workpiece surface in the keyhole welding process. The following equations illustrate the heat sources employed [22–24]. A schematic figure of the geometry and thermal model is shown in Fig. 1.

$$q_v(x,y,z) = \frac{6f\eta p}{\pi r_v^2 d}\ exp\left(-3\frac{(x^2+y^2)}{r_v^2}\right)\left(\frac{mz+r_v}{md+2r_v}\right) \tag{1}$$

$$q_f(x,y,z) = \frac{6\sqrt{3}ff_f\eta p}{a_f bc\pi\sqrt{\pi}} exp\left(-3\left(\frac{x^2}{a_f^2}+\frac{y^2}{b^2}+\frac{z^2}{c^2}\right)\right) \tag{2}$$

$$q_r(x,y,z) = \frac{6\sqrt{3}ff_r\eta p}{a_r bc\pi\sqrt{\pi}}\ exp\left(-3\left(\frac{x^2}{a_r^2}+\frac{y^2}{b^2}+\frac{z^2}{c^2}\right)\right) \tag{3}$$

The energy distribution of the double ellipsoidal heat source at the front and rear of the laser beam is denoted by $q_f$ and $q_r$, respectively, while $q_v$ signifies the energy distribution within the cylindrical heat source. The distribution factors for the energy

**Table 1**
Material chemical composition and mechanical properties of AISI 1060 and DSS 2205 [21].

| Mechanical properties | Yield Tensile Strength (MPa) | | Ultimate Tensile Strength (MPa) | | | Elongation (%) | | | |
|---|---|---|---|---|---|---|---|---|---|
| AISI 1060 (CK60) | 340–700 | | 670–860 | | 4–14 | | | | |
| DSS 2205 | 448 | | 621 | | 25 | | | | |
| Elements | C | Si | Mn | P | Cr | Ni | Mo | S | Fe |
| AISI 1060 (CK60) | 0.61 | 0.40 | 0.75 | 0.03 | 0.40 | 0.40 | 0.10 | 0.035 | balance |
| DSS 2205 | 0.03 | 1.00 | 2.00 | 0.03 | 23.0 | 6.5 | 3.5 | 0.02 | balance |

**Table 2**
Primarily laser welding experiments.

| Row No. | Laser power (W) | Welding speed (mm/min) | Focal distance (mm) | Beam deviation (mm) | Beam energy density (w/cm$^2$) |
|---|---|---|---|---|---|
| 1 | 400 | 300 | 0 | −0.5 | 4.52 |
| 2 | 300 | 400 | 2 | 0.0 | 1.9 |
| 3 | 150 | 300 | 0 | 0.5 | 1.69 |
| 4 | 400 | 200 | 5 | −0.5 | 2.1 |
| 5 | 200 | 300 | 0 | −0.5 | 2.2 |
| 6 | 250 | 200 | 0 | 0.5 | 28 |
| 7 | 550 | 250 | 3 | 0.0 | 3.5 |

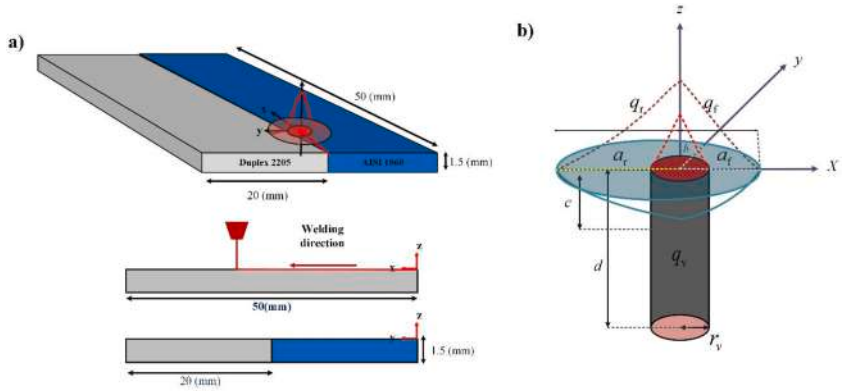


**Fig. 1.** a) Schematic of laser welding simulation, and b) model of heat source.

deposition in the front and rear quadrants of the ellipsoid are represented by $f_f$ and $f_r$. For both the cylindrical heat source and the double ellipsoidal heat source, the energy distribution coefficients are denoted by f. The parameters $a_f$, $a_r$, b, and c, determine the size and shape of the ellipsoid [25,26]. The thickness of the sheets is represented by h. The damping coefficient is denoted by m, and the radius of the heat source is determined by the spot radius. The laser welding power is indicated by P, and the absorption coefficient η is derived based on the emissivity of each workpiece [27].

### 3.1. Governing equations

The field of integrated computing focuses on properly managing and manipulating two distinct physical states of matter: solid and liquid. The governing equations for mass, momentum, and energy in the context of laminar, incompressible flow are presented here [24,28].

Continuity equation:

$$\nabla.\left(\rho\vec{U}\right)=0 \tag{4}$$

Momentum equation:

$$\frac{\partial\left(\rho\vec{U}\right)}{\partial t}+\nabla.\left(\rho\vec{U}\vec{U}\right)=-\nabla p+\nabla.\left(\mu\nabla\vec{U}\right)+\rho\vec{g}-\frac{\mu}{K}\left(\vec{U}\right) \tag{5}$$

$$K=\frac{f_L^3+c}{D(1-f_L)^2} \tag{6}$$

$$f_L=\begin{cases}0 & T\le T_s\\ \dfrac{T-T_s}{T_l-T_s} & T_s<T<T_l\\ 1 & T\ge T_l\end{cases} \tag{7}$$

The final element in the momentum equation represents the Darcy resistance within the mushy region. In the enthalpy-porosity technique, the mushy region behaves as a porous medium, with the porosity of each computation cell being equivalent to the liquid percentage within that cell. In regions that are entirely solid, the porosity is nonexistent, causing the velocity in these regions to be suppressed. Consequently, the momentum suction resulting from the decrease in porosity in the mushy region is incorporated into the momentum equation as the momentum source term. The coefficient K, expressed in terms of porosity, can be determined using the

Kozny-Carman equation [29]. The liquid fraction $f_L$ was defined in order to determine the solid and liquid area. During the phase transition between liquid and solid states, the liquid fraction alternates between the extreme values of 0 and 1. Therefore, by incorporating the liquid portion into the equation for the conservation of momentum, it can account for the force resulting from the transformation of material phases.

Energy equation:

$$\frac{\partial(\rho H)}{\partial t} + \nabla.\left(\rho \vec{U} H\right) = \nabla.(k\nabla T) + q_f + q_r + q_V \tag{8}$$

$k$ is the thermal conductivity coefficient, $H$ is the total enthalpy, $T$ is the temperature.

### 3.2. Boundary conditions

$$k\frac{\partial T}{\partial \vec{n}} = -\varepsilon\sigma\left(T^4 - T_\infty^4\right) - h(T - T_\infty) \tag{9}$$

Boundary condition at the surface of the workpieces:

Shear stress caused by Marangoni flow and surface tension gradient on the surface of the molten pool [30,31]:

$$\mu\frac{\partial u}{\partial z} = -\frac{\partial \gamma}{\partial T}\frac{\partial T}{\partial x} \tag{10}$$

$$\mu\frac{\partial v}{\partial z} = -\frac{\partial \gamma}{\partial T}\frac{\partial T}{\partial y} \tag{11}$$

Where the emissivity coefficient symbolizes $\varepsilon$, the ambient temperature is denoted as $T_\infty$, $\sigma$ represents the Stefan–Boltzmann constant, $h$ signifies the convective heat transfer coefficient, and $\gamma$ is the surface tension parameter.

The thermal boundary conditionality contemplated for the lateral and inferior surfaces incorporates the convective mode of heat transmission and the radiative thermal energy dissipation to the encompassing environment:

$$k\frac{\partial T}{\partial \vec{n}} = -\varepsilon\sigma\left(T^4 - T_\infty^4\right) - h(T - T_\infty) \tag{12}$$

### 3.3. Computational domain

An essential aspect of numerical simulation is accurately determining the computational grid and verifying its independence. Thus, to verify the results regarding the number of distinct elements, the temperature profile at a distance of approximately 25 mm from the starting point of the piece was compared. Based on Fig. 2, it is evident that the outcomes of the grid with 749000 and 812000 elements are nearly identical. As a result, the grid with 749000 cells was chosen.

## 4. Results and discussions

### 4.1. Investigating the laser parameters impact on the maximum depth of melt pool

The results obtained from the analysis of variance (ANOVA) for the experimental data for the depth of the molten pool are shown in

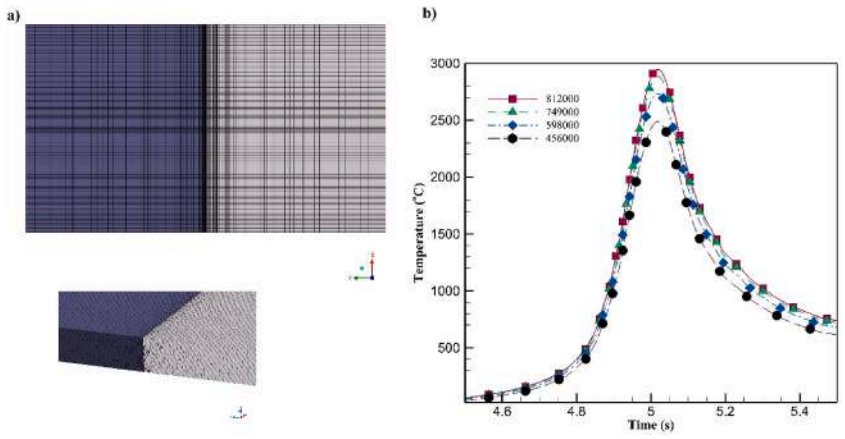


**Fig. 2.** Structured grids, b) Temperature history.

Table 3. According to the F-value and P-value ratio, the two parameters of laser beam deviation and laser power have had a significant effect on the depth of the melt pool. Usually, in the laser welding process, the depth of the molten pool has a direct relationship with the level of laser power absorbed and penetrated on the materials subsurface. Augmentation of the incident beam power could lead to increasing the molten pool depth.

The R-squared value of 90.2 % and Lack of Fit value of 0.70 suggested a strong agreement between the depth of the molten pool regression equation and the experimental data. Equation (13) illustrates the relationship between the process parameters and maximum depth of the dissimilar weld melt pool, including linear, quadratic and interaction terms.

$$\begin{aligned}\text{Depth} = {} & 1.66 + 0.00986\ \text{power} + 0.00373\ \text{speed} + 0.041\ \text{nozzle.dist} + 0.082\ \text{dev} - 0.02418\ \text{nozzle.dist} \times \text{nozzle.dist} \\ & - 0.1869\ \text{dev} \times \text{dev} - 0.000020\ \text{power} \times \text{speed} - 0.000750\ \text{power} \times \text{nozzle} \times \text{dist} - 0.00110\ \text{power} \times \text{dev} \\ & + 0.001150\ \text{speed} \times \text{nozzle.dist} + 0.00250\ \text{speed} \times \text{dev} + 0.0038\ \text{nozzle.dist} \times \text{dev} \end{aligned} \quad (13)$$

As the laser power rises, the greater energy density of the laser beam leads to a surge in the melting volume, beam absorption rate, and penetration efficiency through sheet thickness. This trend leads to the larger dimensions of the melt pool in terms of both depth and width. Measuring the molten pool depth was performed based on the average number of the values adjacent to the DSS 2205 stainless steel fusion line toward the center of the melt pool because of the formation of the bulk of the melt pool from the DSS side. Moving the laser beam towards DSS is marked by value of (+1), as shown in Fig. 3.

Fig. 3 illustrates the impact of the laser power and laser beam adjustment position on the depth of the welded zone. By raising the laser power from 250 to 400 W, the penetration depth of the weld was increased up to 0.5 mm. This increase rate of laser penetration depth was maximum when the laser beam irradiation point was on the DSS side, as compared to the carbon steel part. The maximum depth of laser penetration (about 1.5 mm) was created by irradiating the laser beam on DSS due to the lower melting point of DSS, as compared to the carbon steel.

Fig. 4 illustrates both laser beam position adjustment and nozzle distance on the melt pool depth. It was evident that by decreasing the nozzle distance up to the focal point position of 0 mm, the fusion zone penetration depth was increased due to the irradiation of the laser beam onto the workpiece surface with the highest beam energy density (irradiation of laser beam with minimum beam diameter). With further increase of nozzle distance, because of the reduction in laser beam energy density, the melt pool depth was clearly diminished. The maximum molten pool depth was achieved by deviating the laser beam movement direction to the DSS. This was accomplished by focusing the major portion of beam diameter (the majority of the laser beam energy) on the surface of the DSS, resulting in an increased volume of the melted material on the DSS side because of having a lower melting point and more melting efficiency. By transferring the laser beam about 0.5 mm to the DSS, the molten pool depth experienced a notable increase up to 1 mm. It could be said that higher melding point of carbon steel led to the higher thermal conductivity coefficient of 49.8 W/m. K versus 15 W/m. K for DSS; these could be major reasons explaining the lower participation upon forming the melt pool. The higher thermal conductivity can clearly reduce the melting efficiency of the carbon steel; therefore, the melt volume is clearly decreased by the lower absorbsion of laser beam through carbon steel and lower heating efficiency of DSS by laser heating.

**Table 3**
ANOVA results for dissimilar melt pool maximum depth.

| Source | DF | Adj SS | Adj MS | F-Value | P-Value |
|---|---|---|---|---|---|
| **Model** | 13 | 2.23393 | 0.171840 | 13.15 | 0.000 |
| **Blocks** | 1 | 0.00504 | 0.005042 | 0.39 | 0.543 |
| **Linear** | 4 | 1.51108 | 0.377771 | 28.92 | 0.000 |
| **power** | 1 | 0.72802 | 0.728017 | 55.73 | 0.000 |
| **speed** | 1 | 0.03840 | 0.038400 | 2.94 | 0.106 |
| **nozzle.dist** | 1 | 0.09127 | 0.091267 | 6.99 | 0.018 |
| **dev** | 1 | 0.65340 | 0.653400 | 50.02 | 0.000 |
| **Square** | 2 | 0.30335 | 0.151676 | 11.61 | 0.001 |
| **nozzle.dist×nozzle.dist** | 1 | 0.26608 | 0.266084 | 20.37 | 0.000 |
| **dev×dev** | 1 | 0.06208 | 0.062084 | 4.75 | 0.045 |
| **2-Way Interaction** | 6 | 0.41445 | 0.069075 | 5.29 | 0.004 |
| **power×speed** | 1 | 0.03802 | 0.038025 | 2.91 | 0.107 |
| **power×nozzle.dist** | 1 | 0.09000 | 0.090000 | 6.89 | 0.018 |
| **power×dev** | 1 | 0.01210 | 0.012100 | 0.93 | 0.350 |
| **speed×nozzle.dist** | 1 | 0.21160 | 0.211600 | 16.20 | 0.001 |
| **speed×dev** | 1 | 0.06250 | 0.062500 | 4.78 | 0.044 |
| **nozzle.dist×dev** | 1 | 0.00023 | 0.000225 | 0.02 | 0.897 |
| **Error** | 16 | 0.20901 | 0.013063 | | |
| **Lack-of-Fit** | 12 | 0.13689 | 0.011407 | 0.63 | 0.758 |
| **Pure Error** | 4 | 0.07212 | 0.018031 | | |
| **Total** | 29 | 2.44294 | | | |
| S | R-sq | R-sq(adj) | | R-sq(pred) | |
| 0.114294 | 91.44 % | 84.49 % | | 69.97 % | |

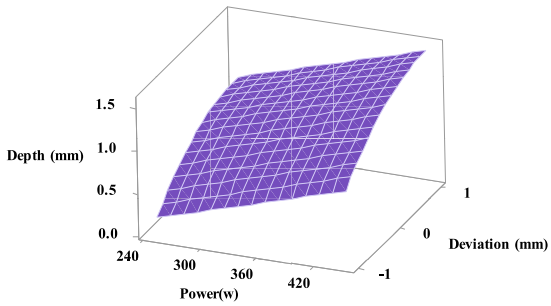


**Fig. 3.** The influence of the laser beam deviation and beam power on melt pool depth.

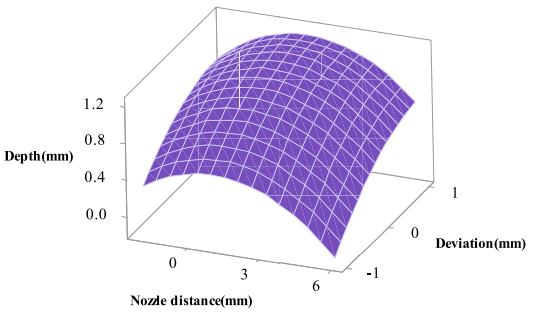


**Fig. 4.** The influence of nozzle distance and beam deviation on melt pool depth.

### *4.2. Investigating the laser parameters effect on dissimilar joint tensile strength*

The ANOVA results obtained for the tensile strength of the dissimilar joint can be observed in Table 4. The tensile strength of the dissimilar joint was significantly altered by the laser power and linear movement speed because of having the minimum p-value and a higher F-value. Generally, the peak value of the tensile strength was achieved when the laser beam was irradiated at the center of the joint. Every deviation toward each material can weaken the joint tensile strength due to the non-homogenous mixing of the material, although the weld penetration may be complete. The R-sq 90.2 % and lack of fit 0.368 imply that the regression equation of tensile

**Table 4**
The ANOVA results for tensile strength of the joint.

| Source | | DF | Adj SS | Adj MS | F-Value | P-Value |
|---|---|---|---|---|---|---|
| **Model** | | 13 | 131552 | 10119.4 | 11.10 | 0.000 |
| **Blocks** | | 1 | 12 | 12.1 | 0.01 | 0.910 |
| **Linear** | | 4 | 110624 | 27655.9 | 30.34 | 0.000 |
| **power** | | 1 | 96520 | 96520.2 | 105.90 | 0.000 |
| **speed** | | 1 | 12604 | 12604.2 | 13.83 | 0.002 |
| **nozzle.dist** | | 1 | 683 | 682.7 | 0.75 | 0.400 |
| **dev** | | 1 | 817 | 816.7 | 0.90 | 0.358 |
| **Square** | | 2 | 14458 | 7229.2 | 7.93 | 0.004 |
| **nozzle.dist×nozzle.dist** | | 1 | 537 | 536.7 | 0.59 | 0.454 |
| **dev×dev** | | 1 | 14360 | 14360.0 | 15.76 | 0.001 |
| **2-Way Interaction** | | 6 | 6457 | 1076.2 | 1.18 | 0.365 |
| **power×speed** | | 1 | 784 | 784.0 | 0.86 | 0.367 |
| **power×nozzle.dist** | | 1 | 756 | 756.3 | 0.83 | 0.376 |
| **power×dev** | | 1 | 1369 | 1369.0 | 1.50 | 0.238 |
| **speed×nozzle.dist** | | 1 | 1764 | 1764.0 | 1.94 | 0.183 |
| **speed×dev** | | 1 | 20 | 20.2 | 0.02 | 0.883 |
| **nozzle.dist×dev** | | 1 | 1764 | 1764.0 | 1.94 | 0.183 |
| **Error** | | 16 | 14583 | 911.4 | | |
| **Lack-of-Fit** | | 12 | 11958 | 996.5 | 1.52 | 0.368 |
| **Pure Error** | | 4 | 2625 | 656.2 | | |
| **Total** | | 29 | 146134 | | | |
| S | R-sq | R-sq(adj) | | R-sq(pred) | | |
| 1.72382 | 90.20 % | 83.28 % | | 71.77 % | | |

strength could be well aligned with the data obtained from the experiments. Equation (14) illustrates the correlation between process parameters and the joint's tensile strength.

$$\begin{aligned}\text{Tensile} = & -138 + 1.831\ \text{power} + 0.73\ \text{speed} + 3.9\ \text{nozzle.dist} - 108\ \text{dev} - 1.09\ \text{nozzle.dist} \times \text{nozzle.dist} - 89.9\ \text{dev} \times \text{dev} \\ & - 0.00280\ \text{power} \times \text{speed} + 0.0688\ \text{power} \times \text{nozzle.dist} + 0.370\ \text{power} \times \text{dev} - 0.1050\ \text{speed} \times \text{nozzle.dist} + 0.045\ \text{speed} \\ & \times \text{dev} - 10.50\ \text{nozzle.dist} \times \text{dev}\end{aligned} \tag{14}$$

Fig. 5 illustrates the impact of laser power and welding speed on the tensile strength of the welded joint. Evidently, as the laser power was raised from 250 to 400 W, the tensile strength of the dissimilar welded joint was significantly increased from 300 MPa to 550 MPa. This value was about 45 percent of the average tensile strength value for the dissimilar joint.

The rise of welding speed resulted in a reduction of the tensile strength of the joint at the laser power of 400 W, specifically by approximately 40 MPa, which was about 10 percent. Hence, it could be concluded that by raising the beam power, the maximum tensile strength of the dissimilar joint was enhanced as a result of the larger volume of the melt and a progressive rise in the penetration depth of the weld.

In contrast to the laser power, the effect of increasing the welding speed on the tensile strength was insignificant and negligible.

The effect of the welding speed and nozzle distance on the tensile strength of the welded joint can be observed in Fig. 6. With the increase of the welding speed, the tensile strength was always decreased, but this decrease in tensile strength at the focal point was 30 MPa, while it was reduced to 150 MPa by boosting the nozzle height about 6 mm. On the contrary, when welding at the low speed of 200 mm/min, the rise in the nozzle distance led to the partial enhancement of approximately 20 percent in the tensile strength of the welded joint, as depicted in Fig. 6. Due to the longer laser beam interaction time with the surface of the workpiece, a higher melt volume was created at the weld joint, in comparison to the focal point position at the welding speed of 200 mm/min. The highest rate of decrease in mechanical strength was observed with increasing the welding speed at the nozzle distance of 6 mm, which was reduced by augmenting the nozzle distance and welding speed due to a notable reduction in the melt volume and weld penetration depth in the middle of the fusion zone of the two dissimilar metals components. It can be, therefore, said that changes in the welding speed at the focal point position do not remarkably alter the penetration depth of the weld and hence, the mechanical strength of the workpiece. This is caused by the sufficient density of laser beam energy and the melted material volume has not been significantly changed by variation of the laser welding speed. Laser welding at the nozzle distance of 3 mm and 6 mm, due to the application of lower energy density, reduces the penetration depth of the weld and the tensile strength of the workpiece, while it increases the welding speed.

Fig. 7 depicts the tensile strength variation of the welded joint with the laser power and beam deviation. It could be seen that by welding at the focal point, the highest rate of tensile strength was obtained, which was up to about 550 MPa. By moving the laser beam into the direction of the carbon steel, the maximum tensile strength was decreased from 540 MPa to 340 MPa (strength reduction amount was about 200 MPa). Meanwhile, with the laser beam deviation toward DSS, there was no reduction in the rate of tensile strength. Due to the lower thermal conductivity of DSS, when the laser beam was deflected into the DSS side, the carbon steel was also melted due to the higher heat conduction of the carbon steel and more heat accumulation in the DSS; also, its melting volume was almost near the state where laser welding was performed at the junction of two parts.

Therefore, by moving the laser beam towards the DSS, in addition to melting it, the carbon steel was sufficiently melted and a suitable tensile strength was obtained for the connection. When the laser beam deviated towards the carbon steel, due to its higher heat conductivity, the melting volume in the connection area of the two parts was reduced and the melting volume of the DSS was significantly reduced, which caused a decrease in the tensile strength of the work piece.

### 4.3. Investigating the effect of laser parameters on the elongation rate of the joint

The ANOVA results related to elongation can be observed in Table 5. The strain rate of the dissimilar joint was significantly affected by laser beam incident position adjustment and the power of the laser. Additionally, the relationship between laser beam deviation and nozzle distance stood out as one of the most significant among all interaction parameters. The regression equation of elongation could

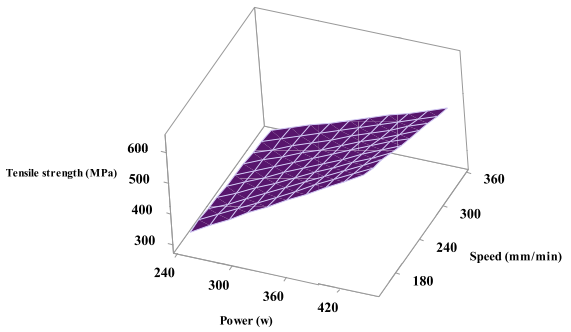


**Fig. 5.** The laser power welding speed impact on the joint tensile strength.

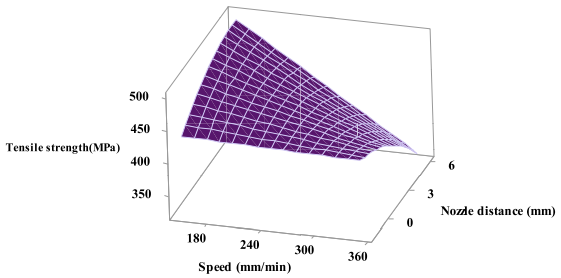


**Fig. 6.** Tensile strength variation with welding speed and nozzle distance.

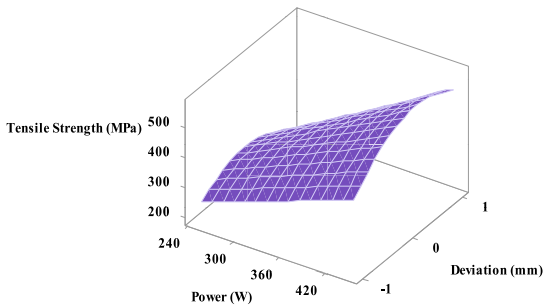


**Fig. 7.** Effect of laser power and beam deviation on the tensile strength of the joint.

be adequately fitted with the experimental data, according to the Rsq of 90 % and lack of fit 0.9. Equation (15) includes the linear, quadratic and interaction terms of the laser welding parameters.

$$\begin{aligned}\text{Elongation} = {} & 10.45 + 0.0500\ \text{power} - 0.0367\ \text{speed} + 0.20\ \text{nozzle.dist} + 17.50\ \text{dev} - 0.1641\ \text{nozzle.dist} \times \text{nozzle.dist} \\ & - 9.13\ \text{dev} \times \text{dev} - 0.00750\ \text{power} \times \text{nozzle.dist} - 0.0350\ \text{power} \times \text{dev} \\ & < +0.01000\ \text{speed} \times \text{nozzle.dist} + 0.0050\ \text{speed} \times \text{dev} - 1.250\ \text{nozzle.dist} \times \text{dev} \end{aligned} \quad (15)$$

Fig. 8 illustrates how the elongation rate of the weld joint was influenced by both beam power and incident beam position

**Table 5**
The ANOVA results for elongation of the joint.

| Source | DF | Adj SS | Adj MS | F-Value | P-Value |
|---|---|---|---|---|---|
| **Model** | 12 | 464.850 | 38.737 | 13.04 | 0.000 |
| **Blocks** | 1 | 30.817 | 30.817 | 10.37 | 0.005 |
| **Linear** | 4 | 218.833 | 54.708 | 18.41 | 0.000 |
| **power** | 1 | 73.500 | 73.500 | 24.73 | 0.000 |
| **speed** | 1 | 16.667 | 16.667 | 5.61 | 0.030 |
| **nozzle.dist** | 1 | 32.667 | 32.667 | 10.99 | 0.004 |
| **dev** | 1 | 96.000 | 96.000 | 32.31 | 0.000 |
| **Square** | 2 | 152.700 | 76.350 | 25.69 | 0.000 |
| **nozzle.dist×nozzle.dist** | 1 | 12.250 | 12.250 | 4.12 | 0.058 |
| **dev×dev** | 1 | 148.028 | 148.028 | 49.81 | 0.000 |
| **2-Way Interaction** | 5 | 62.500 | 12.500 | 4.21 | 0.011 |
| **power×nozzle.dist** | 1 | 9.000 | 9.000 | 3.03 | 0.100 |
| **power×dev** | 1 | 12.250 | 12.250 | 4.12 | 0.058 |
| **speed×nozzle.dist** | 1 | 16.000 | 16.000 | 5.38 | 0.033 |
| **speed×dev** | 1 | 0.250 | 0.250 | 0.08 | 0.775 |
| **nozzle.dist×dev** | 1 | 25.000 | 25.000 | 8.41 | 0.010 |
| **Error** | 17 | 50.517 | 2.972 | | |
| **Lack-of-Fit** | 13 | 27.767 | 2.136 | 0.38 | 0.920 |
| **Pure Error** | 4 | 22.750 | 5.688 | | |
| **Total** | 29 | 515.367 | | | |
| | S | R-sq | R-sq(adj) | R-sq(pred) | |
| | 1.72382 | 90.20 % | 83.28 % | 71.77 % | |

adjustment. The amount of weld elongation was directly increased with the rise of laser power. Raising the laser power from 200 to 400 W resulted in a 10 % increase of the strain rate, which was half of the maximum domain of the elongation rate. The highest strain rate was obtained when the laser beam was irradiated at the junction of two parts, which increased the strain rate to about 18 %; meanwhile, every deviation toward DSS and carbon steel had a reduction of the strain rate, which was about 8 % and 22 %, respectively. It could be, therefore, said that the highest amount of strain rate was created at the center of the dissimilar weld joint, which was due to the creation of a proper connection and the maximum participation of both materials to form the melt pool composed of melting and the efficient fusion of dissimilar materials.

Fig. 9 illustrates the impact of variations in the linear speed of welding and deviation of the laser beam on the elongation rate of the weld joint. The highest elongation rate during welding was at the center point between two parts; when the laser beam was deflected towards DSS or carbon steel, the strain rate was decreased.

When the laser beam was deviated about 0.5 mm towards the carbon steel, due to the higher energy intensity, a severe thermal gradient was created in the carbon steel workpiece, thereby increasing the percentage of the fully martensite phase formation due to the rapid cooling. Therefore, although the formation of martensite structure increases the tensile strength to some extent, it generally reduces the strain rate by cracking and brittle fracture. Therefore, the weld joint plastic deformation is reduced due to the formation of the more brittle failure of the weld joints. It could be clearly seen that this effect is reduced by deviating the laser beam in the direction of DSS. The reason is the decrease in the volume of the martensite phase from the fusion zone. By deflecting the laser beam towards the DSS, the strain rate was increased by 10 %. Therefore, it could be said that the strain rate was tripled when the beam was deflected from carbon steel towards DSS. The maximum elongation rate was gained when the laser beam was irradiated at the center of two parts, where the fusion zone had been composed of two materials melted and had a higher ductile deformation rate. Deviation of the laser beam toward DSS, while producing the weld bead with the full penetration depth, led to the fracture of the welded joint from the fusion line of the carbon steel because of the insufficient melting of the carbon steel and its contribution to the formation of the fusion zone.

### *4.4. Microstructural analysis of the weld joint*

The microstructural analysis was done from both base metals toward the center of the fusion zone area of the dissimilar joint of carbon steel and DSS. Fig. 10 shows the size of the molten pool and its expansion in two base metals. As can be seen in Fig. 10a, slight microstructural changes could be observed at the narrow region of the DSS side heat affected zone adjacent to the fusion line of the dissimilar joint. On the other hand, it could be seen that there were no microstructural changes near the border of the molten pool with the carbon steel; so it could be said that there was a separation zone in the border line of the molten pool with carbon steel. The most important reason is the higher melting point of carbon steel, which was as much as 100 °C, causing the formation of more melting volume of the molten pool of DSS.

Fig. 10c represents the microstructure of DSS that consisted of a ferrite matrix in which austenite grains had been distributed. Fig. 10d also shows the microstructure of AISI 1060 carbon steel, which mainly consisted of the martensitic microstructure.

In general, the changes in the microstructure of the melt pool area and base metals are affected by the thermal cycles induced by heating and high cooling rate applied in the area of the molten pool and the adjacent region near the heat affected zone of the base metals. According to Fig. 11, the changes of the microstructure in the melt pool and the surrounding regions were influenced by the heating and cooling cycles experienced within the melt pool area of DSS 2205. Increasing the temperature beyonf the melting point followed by rapid cooling with variable temperature gradient from the center of the molten pool to the base metal caused a different microstructure. In Fig. 11-a, it could be seen that the distribution of ferrite-austenite in the heat affected zone of DSS had been changed, leading to the formation of the austenitic phase. In general, the microstructure of the heat affected zone includes austenite phases and δ ferrite grains. Due to the lower temperature gradient, compared to the center of the molten pool (receiving a lower heating intensity), as a result of the overall decrease in the cooling rate, relative to the fusion zone center, there was a clear rise due to the formation of the austenite phase, as also stated in another study [32].

Most the microstructure in the fusion zone was typically formed through the solidification process of DSS. Depending on different temperature gradients and thermal variable conductivity coefficient according to the temperature gradient, the molten pool microstructure seemed different. Due to the higher cooling rate, columnar dendritic and inter-dendritic microstructures had been created in

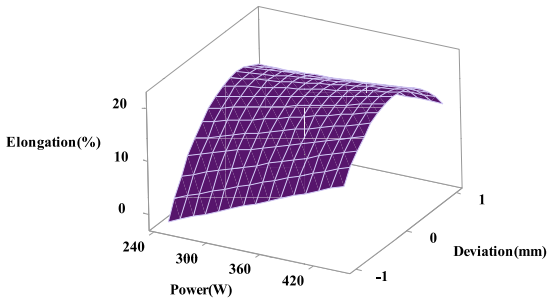


**Fig. 8.** The joint elongation rate with laser power and beam deviation.

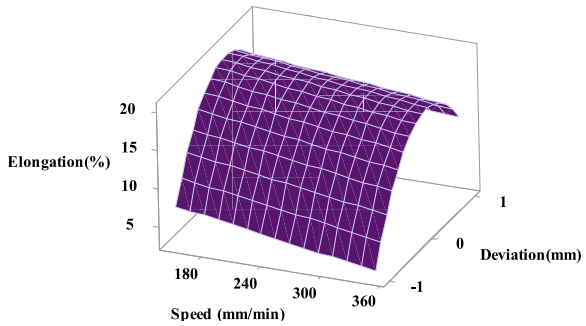


**Fig. 9.** Effect beam deviation and speed of welding on the elongation rate of the joint.

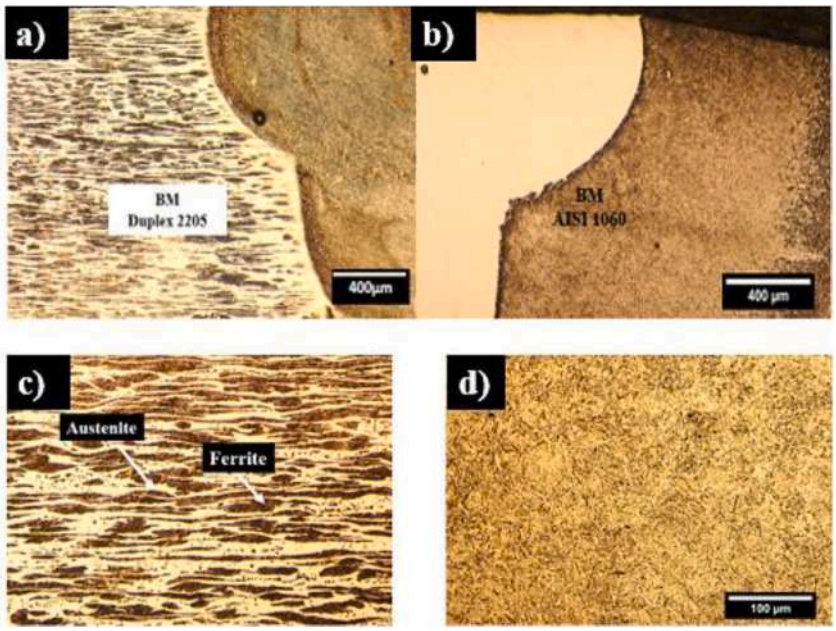


**Fig. 10.** Microstructure of weld joint for a) DSS side of fusion zone, b) carbon steel base metal of fusion zone, c) DSS microstructure, d) AISI 1060 microstructure.

the vicinity of the boundary line area of the molten pool with the DSS base metal, as could be evidently observed in Fig. 11b and c. By increasing the distance from the boundary line of the molten pool and moving towards the center of the pool, due to the higher heating rate and the lower cooling rate, mainly the cellular microstructure with epitaxial grain growth was observed. In some cases, the presence of porosity in the molten pool near the base metal of DSS could be seen, as shown in Fig. 11c.

In Fig. 12, the microstructure of the molten pool was completely shown from the DSS side to the carbon steel side. Comparison of Fig. 12a and b showed that the distribution of the cellular dendritic microstructure had been increased in the fusion zone center region directed to the carbon steel side. In the region of the boundary line of the fusion zone adjacent to the carbon steel, a finer-grained columnar dendritic microstructure could be seen, as compared to the region inclined towards DSS. In Fig. 12c, inter-dendritic microstructure and grains with epitaxial growth could be seen in the area close to DSS; meanwhile, in the area close to carbon steel, an only cellular and columnar dendritic microstructure was observed. At the fusion line between the fusion zone and the carbon steel base metal, a narrow region separated from the carbon steel fusion zone microstructure could be observed, as shown in Fig. 12d. The higher melting temperature of carbon steel caused the formation of a separate area at the fusion line of carbon steel, which occurred due to the insufficient melting of carbon steel and rapid solidification rate due to the high heat thermal conductivity coefficient of carbon steel. Furthermore, the number of porous holes in the molten pool towards the carbon steel was clearly more than that in the area near DSS. The higher thermal conductivity of carbon steel, which was about 49.8 W/m. K, as compared to 15 W/m. K for DSS, could induce such phenomena.

In Fig. 12c, inter-dendritic microstructure and grains with epitaxial growth could be seen in the area close to DSS, while in the area close to carbon steel, an only cellular and columnar dendritic microstructure was observed (see Fig. 12b). There was a narrow region separated from the molten pool microstructure that could be seen at the fusion line between the molten pool and the carbon steel base

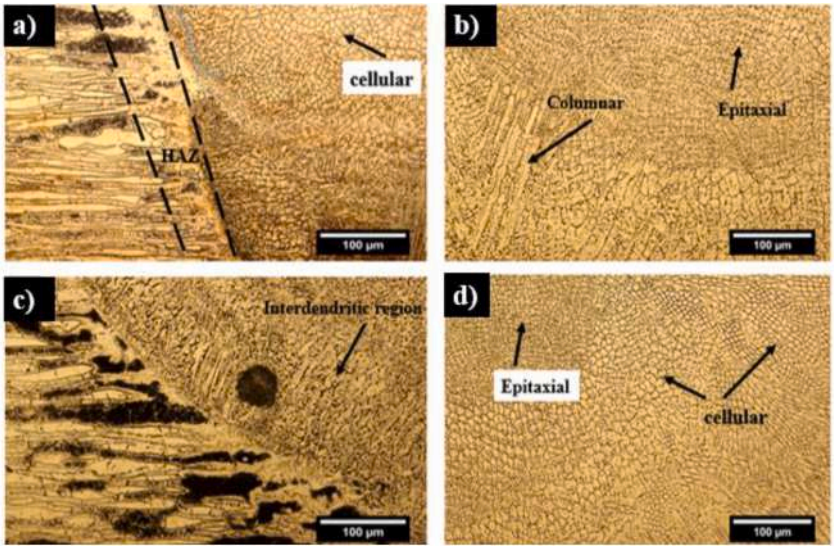


**Fig. 11.** The fusion zone microstructure at different regions for a) HAZ of DSS, b) center of fusion zone, c) lower section of fusion zone adjacent to the DSS, d) upper part of the fusion zone at center line of the weld bead.

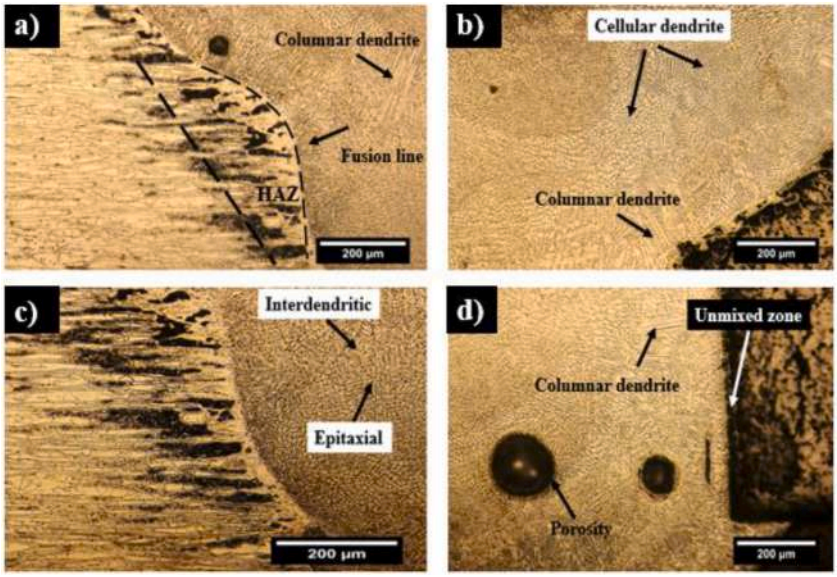


**Fig. 12.** Microstructure of fusion zone near the fusion line regions for a) DSS, b) AISI 1060 carbon steel, c) bottom region of fusion zone adjacent to the DSS, d) lower part of the fusion zone near the carbon steel fusion line.

metal, as can be seen in Fig. 12d. The higher melting temperature of carbon steel caused the formation of a separate area at the fusion line of carbon steel, which occurred due to the insufficient melting of carbon steel and rapid solidification rate owing to the high thermal conductivity of the carbon steel. Furthermore, the number of porous holes in the molten pool towards the carbon steel was clearly more than that in the area near DSS.

### *4.5. Numerical simulation results validation for the temperature field*

The temperature distribution from the base metals to the weld fusion zone was investigated via the numerical simulation method. The temperature distribution by variation of laser power is depicted in Fig. 13 via numerical simulation. As shown in Fig.13a–c, by increasing the laser power from 250 to 400 W, the extension of the high temperature region (more than 1800 °C) was raised to about 150 percent at both depth and width. Due to the higher thermal conductivity rate of AISI 1060 steel (more than 3 fold), the extension of the region with a temperature higher than 300 °C was clearly more than that in the DSS side. On the other hand, there was no

remarkable discrepancy between the high temperature region (more than 1600 °C) at both sides of metals. Additionally, at the DSS side, the high temperature region was extended more than AISI 1060 because of the lower thermal conductivity coefficient and the lower melting point of about 100 °C. Therefore, the wider region including the heat affected zone and the melt pool at the upper part of the weld melt pool region and adjacent areas was formed, as compared to the AISI 1060 steel.

Fig. 14 evidently depicts the temperature distribution from the top surface of the dissimilar welded joint. It was vividly observed that by increasing the laser power from 250 to 400 W (see Fig. 14a–c), the low temperature (below 450 °C) was diffused with higher intensity through AISI 1060 steel. The region was extended about 1.5 fold of DSS because of the higher thermal conductivity coefficient. There was a slight discrepancy between the temperature distribution toward DSS 2205 and AISI 1060 steel. The region with the threshold temperature higher than 1200 °C seemed to be more at the DSS side at the weld top surface.

Fig. 15 illustrates the comparison of the experimental and numerical results for the melt pool dimension and shape at both sides of the base metals. It was evidently observed that the melt pool extension toward each base metal significantly differed from each other because of having different thermophysical properties, including thermal conductivity and melting point. Considering the experimental and numerical simulation results can lead to a good agreement between them for melt pool geometry. As depicted in Fig. 15 a to 15c, a notable difference at the melt pool width from the upper to lower part of the melt pool width at the DSS side implied that the lower heat conduction coefficient accumulated the melted material at the upper part of the melt pool; this was apart from different melt flow mechanisms and characteristics predominated on the thermophysical characterization of different materials. On the contrary, based on the comparison of Fig. 15b and c, it could be concluded that the melt pool width had experienced lower variation at the AISI 1060 side. One of the major reasons could be the higher thermal conductivity rate at the AISI 1060 steel side which extended the melt pool width at the lower part of the melt pool, as compared to the DSS side. Additionally, the comparison of the experimental and numerical results for the melt pool depth, as shown in Fig. 15c, implied that the penetration depth at the high level of laser power at the AISI 1060 steel side was clearly higher than that in the DSS side.

Fig. 16 illustrates the relation between the temperature distribution and melt flow variation (dimension and shape) in case the laser beam deviated toward both base metals. When the laser beam deviated toward DSS 2205 side (see Fig. 16a and c), the melt pool was mostly formed with the narrow region of the melting region at the carbon steel side from half of the workpiece thickness. Furthermore, the penetration depth of the melt pool was nearly complete when the laser beam deviated about 0.5 mm to the DSS side. Lower melting point and thermal conductivity coefficient incredibly increased the melting efficiency at the DSS side. The experimental results obtained for the relation between the laser beam deviation and beam power on the melt pool depth (presented in Fig. 3) were in agreement with the numerical simulation ones. When the laser beam deviated about 0.5 mm toward AISI 1060 side (see Fig. 16b and d), the lower heat dissipation and smaller melt pool geometry (width and depth) were clearly observed. Evidently, the higher thermal conductivity coefficient of AISI 1060 steel reduced the extension of the melt pool at both width and depth base metal. At this condition, the melt pool extended toward DSS from a third of the workpiece thickness, as shown in Fig. 16d.

### 4.6. *Mechanical properties of dissimilar weld joints*

The mechanical properties of dissimilar welding joints of carbon steel and DSS were investigated by evaluating the tensile strength, strain rate and failure analysis of the tensile samples' cross section. Each test was repeated three times and the impact of changes in laser power and distance of the nozzle on the failure mechanism of the joint was investigated.

The appearance of tensile test samples can be seen in Fig. 17. In Fig. 17a–c, the effect of increasing the laser power can be observed. In Fig. 17d–f, the effect of the nozzle distance on the fracture surface of the workpiece was evaluated. According to the tensile tests conditions, as can be seen in Fig. 17g–l, the tensile test samples failed from the heat affected zone adjacent to the carbon steel. It could be clearly observed that most of the samples failed from the region between the molten pool fusion line and the carbon steel base metal

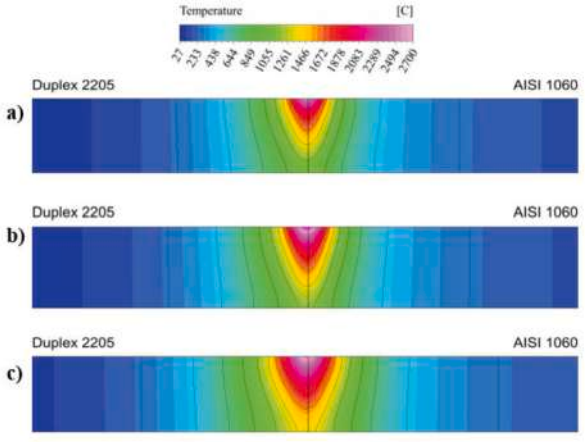


**Fig. 13.** The cross section temperature field of duplex2205/AISI 1060 joint at different laser power of a) 250W, b) 300W, c) 400W.

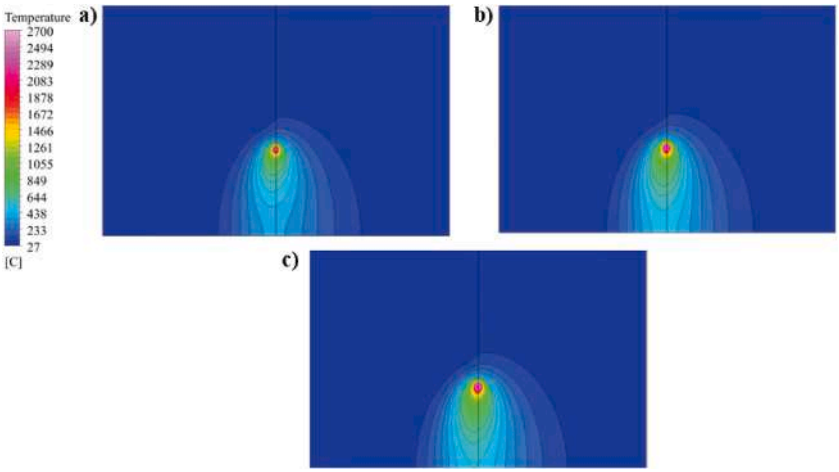


**Fig. 14.** The top section temperature field of duplex2205/AISI 1060 joint at different laser power of a) 250 W, b) 300 W, c) 400 W.

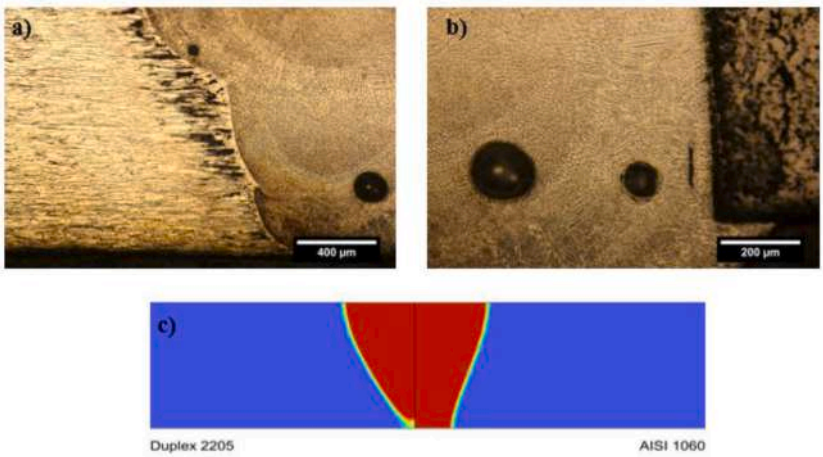


**Fig. 15.** Melt pool geometry and shape for a) DSS side experiment, b) AISI 1060 experiment, c) melt flow at laser power of 500 W.

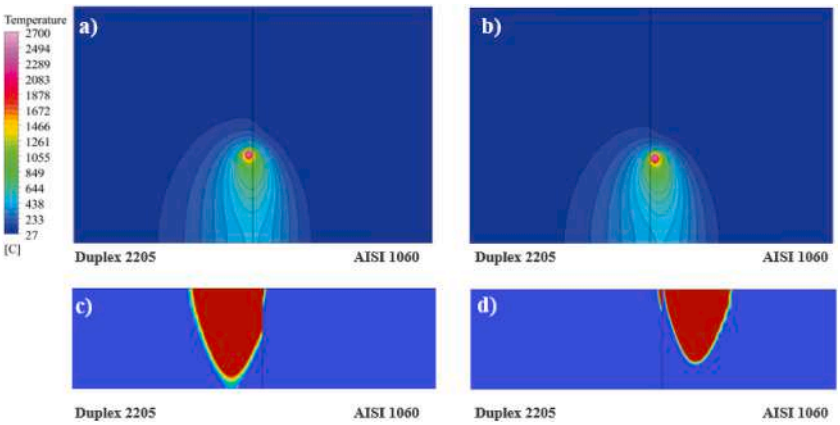


**Fig. 16.** The top section temperature field of duplex 2205/AISI 1060 joint at different laser power of a) 250 W, b) 300 W, c) 400 W.

due to the separation zone at the boundary of the molten pool zone adjacent to the carbon steel. When the focal distance was extended, as a result of the lack of enough penetration and insufficient melt volume and the presence of the separation zone on the side of the carbon steel, this failure mechanism was predominant among most of the samples.

In Fig. 18, the fracture surface of the welded samples is visible at various levels of laser power. By increasing the laser power from 300 to 400 W, t deeper-depth cavities were formed on the cross-section surface of the failed samples, thus suggesting a greater melting volume and a stronger connection.

Fig. 18a–c shows the fracture surface of carbon steel, with a brittle fracture mechanism due to the martensitic nature of the microstructure of carbon steel. Fig. 18d–f also illustrate the fracture cross-section of the DSS part, showing a mostly ductile fracture mode when compared to carbon steel. Furthermore, the depth of fracture holes was greater, which indicated the creation of a higher volume of the melted material on the DSS side.

Fig. 19 illustrates the comparison of tensile stress and strain rate of both base metals. The big difference between these two graphs related to the strain rate of them. As shown in Fig. 19a, AISI 1060 had the maximum strain rate of 0.35 % and the ultimate tensile stress of 610 MPa. On the contrary, DSS 2205 had about 18 percent of elongation and tensile strength of 560 MPa (see Fig. 19b). It can be said that DSS had a ductile fracture mechanism with a high elongation rate, while AISI 1060 had a more brittle fracture mechanism. The effect of laser power on the joint tensile stress could be observed in Fig. 20. At the laser power of 250 W, the maximum tensile stress was about 350 MPa with the strain rate was 7 percent. Increasing the laser power up to the 350 W significantly raised the stress to the value of 490 MPa and the strain rate to 12 percent. Further increase of the laser power remarkably augmented the strain rate to about 21 percent, while a slight increase in tensile stress was observed. The main reason behind increasing the tensile stress by raising the laser power from 250 to 350 W could be the notable increase of weld penetration (melt pool depth) and therefore, the melt volume. The evident increase of strain rate from 12 to 21 percent was mainly related to the formation of the coarser grain size of the cellular microstructure and more tempered martensitic microstructure formed at the fusion zone toward the AISI 1060 side. It could be said that the higher laser power density ended in the more ductile fracture mechanism of the weld joint. Another point that could be noted here is the fact that by using a laser power density more than 0.05 MW/cm$^2$, the clear microstructural changes (cellular dendrite grain coarsening along with formation tempered martensite) had a significant influence on the fracture mechanism of the tensile tests samples from a brittle one to a ductile one.

The microhardness profile of the welded joints for two different laser powers is shown in Fig. 21. Generally, by increasing the laser power to 450 W, the hardness profile of the fusion zone was clearly higher. Near the fusion line of the DSS, the hardness was increased about 50 HV, while at the center of the fusion zone, the maximum increase rate reached to 250 HV. At the fusion line of the melt pool toward AISI 1060, the hardness was reduced sharply and this trend was continued to reach the hardness of the AISI 1060 base metal. In the case of welding at 400 W, the microhardness profile of the fusion zone had an incremental trend, while its trend was reversed near the AISI 1060 fusion line. From the HAZ of AISI 1060 toward the base metal, the hardness was reduced abruptly due to the formation of the tempered martensitic phase. Near the fusion line of both metals, a columnar dendrite microstructure was formed and it was transformed to the fine grained cellular microstructure at the center of the fusion zone (see Fig. 22a and c). By increasing the distance

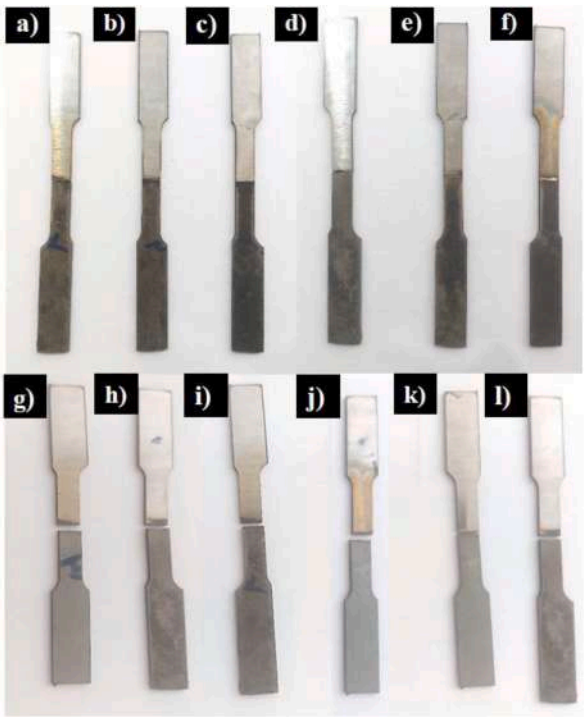


**Fig. 17.** Appearance of tensile tests samples at focal length of 0 mm, welding speed 200 mm/min, for laser power of a) 300W, b) 350W, c) 400W, laser power of 400W for focal length of d) 0 mm, e) 2 mm, f) 4 mm and the fracture appearance of tensile tests samples for laser power of g) 300W, h) 350W, i) 400W, laser power of 400W for focal length of j) 0 mm, k) 2 mm, l) 4 mm.

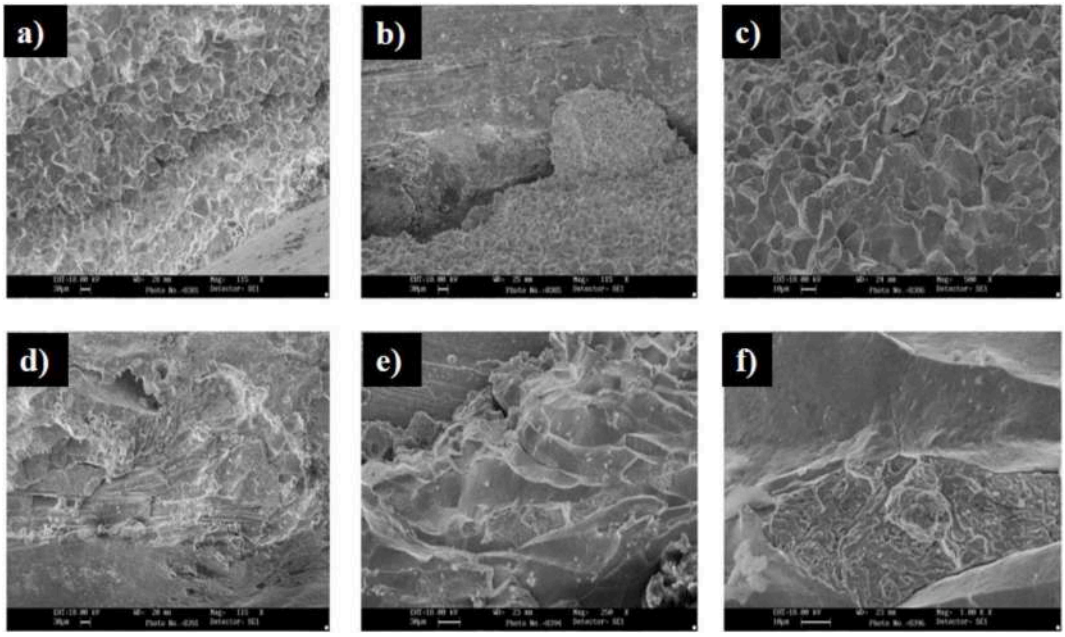


**Fig. 18.** Tensile tests samples fracture surface appearance at welding speed of 200 mm/min, for laser power of a) 300W, b) 350W, c) 400W, laser power of 400W for d) 0 mm, e) 2 mm, f) 4 mm.

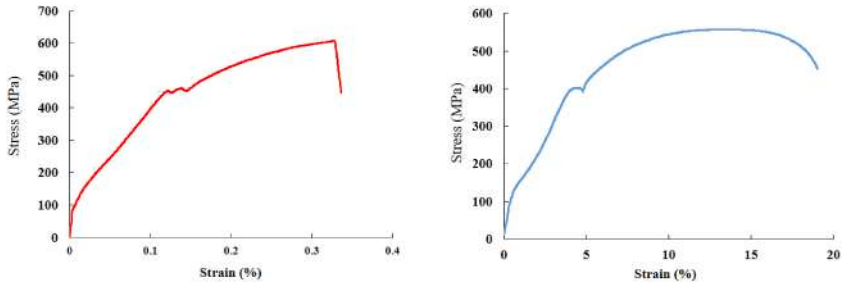


**Fig. 19.** Tensile stress/strain graphs of base metals for a) AISI 1060, b) DSS 2205.

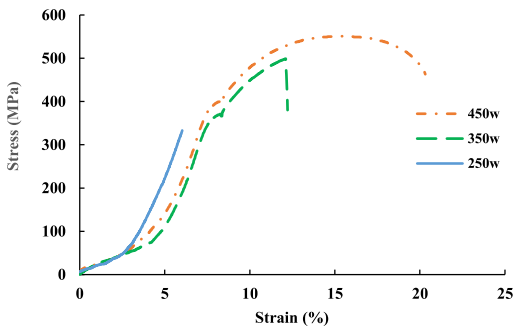


**Fig. 20.** Tensile stress/strain graphs of dissimilar weld joint at different laser power levels.

from the center of the fusion zone toward base metals, the coarse grain microstructure was formed. It should be noted that higher temperature gradient of 450 W laser power clearly reduced the microhardness values from the center of the fusion zone to the AISI 1060 base metal because of the formation of the coarser grain cellular microstructure and the more tempered martensitic microstructure, as shown in Fig. 22b and d. It should be noted that by using the laser power of 400 W, the microhardness fluctuation was evidently reduced.

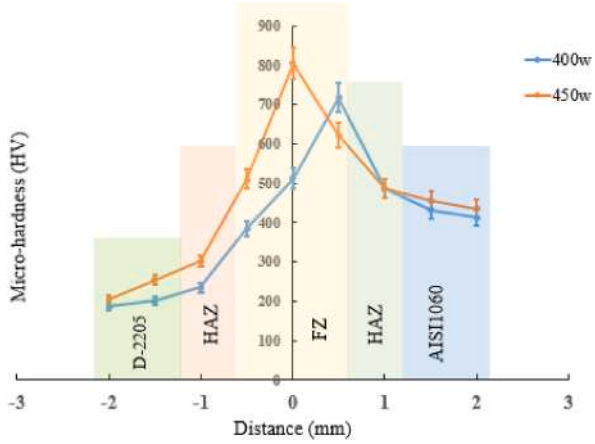


**Fig. 21.** Microhardness of weld joints at different laser power.

To make a comparison between the results of this study and those obtained in the previous research, some of the most relevant results have been evidently outlined to further highlight the similarities and differences. Karimi et al. [19] investigated the effect of fiber laser welding parameters on tensile strength, depth of the melt pool, microstructure and temperature near the laser welding region of dissimilar A516 low carbon steel and DSS. The maximum tensile strength of 500 MPa and 18 percent elongation were obtained at the laser power of 400 W, welding speed of 300 mm/min and the focal point. Additionally, they showed that, through applying higher laser energy density, the fracture ductility of the welded samples was effectively improved. In comparison to their results, the higher laser power at the focal length could lead to the highest tensile stress value. The clear difference between two studies is changing the fracture surface mode from the brittle one to the ductile one by using A516 steel and higher laser power. There was not an evident change in the fracture mode from the brittle one to the ductile one by increasing the laser power through using AISI 1060 base metal.

Kose et al. [33] also investigated dissimilar laser welding of AISI 420 martensitic stainless steel to AISI DSS 2205 sheets by applying the Post-weld heat treatment to the laser-welded joint to analyze the mechanical properties of a welded joint. They reported that by using heat treatment, the retained austenite phase fraction was increased in the microstructure of both martensitic stainless steel and duplex stainless steel. They noticed that the tensile strength of the heat-treated welded joint was improved, but their impact on toughness was decreased. It was found that the tensile strength of the welded joint was lower than that of the base metal. In the present study, the tensile strength of welded joints samples was always lower than that of both base metals, which was close to the results reported in.

Hamada et al. [34] also evaluated the mechanical performance and formability of dissimilar laser welded butt joints between

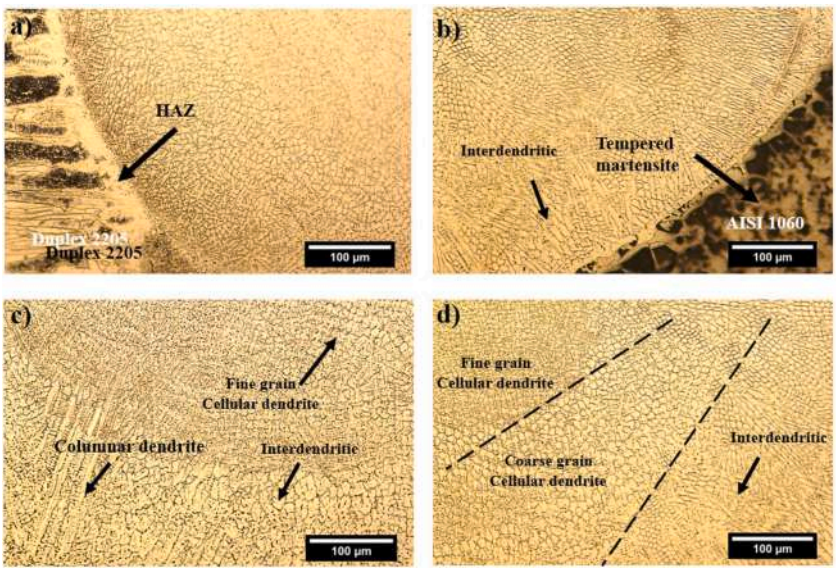


**Fig. 22.** The microstructure of fusion zone and adjacent regions at focal distance and laser power of 450 W for a) DSS 2205 side, b) AISI 1060 side, c) near fusion line of DSS side to the center of the fusion zone, d) near the AISI 1060 fusion line to the center of the fusion zone.

medium stainless steel and high-strength carbon steel. They reported that a fully martensitic microstructure was promoted in the fusion zones processed with the low and high specific point energy of 25, and 30 J. As a result, the hardness values of the fusion zone were slightly decreased by using high specific energy. The tensile properties were not affected since failure occurred at the softer base metal. On the contrary, in this study, the samples' failure was mainly from the unmixed zone toward the carbon steel side and increasing the power density evidently improved the tensile strength of the joints.

## 5. Conclusion

The impact of dissimilar laser welding parameters on the resultant microstructural changes, weld geometry, and mechanical characterizations of the dissimilar joint was analyzed by experimental design. Through adjusting the incident laser power to the workpiece surface, linear movement speed, distance of nozzle from the focal point, and beam deviation for each material, the statistical analysis of the weld joint characterization was conducted and the results were reported as follow:

- The depth of the molten pool is primarily influenced by two factors: the power of the laser and beam deflection. The laser beam deviation on the DSS side is responsible for creating the maximum depth of laser penetration, which is approximately 1.5 mm. On the other hand, when the laser beam is directed towards the carbon steel, it results in a decrease of about 200 MPa in the maximum tensile strength. On the contrary, by moving the laser beam towards the DSS, in addition to melting the DSS, the carbon steel is sufficiently melted and a suitable tensile strength is obtained for the connection.
- The maximum tensile strength of 550 MPa was obtained at the focal point. By laser welding at the focal point, changes in welding speed do not have much effect on the penetration depth of the weld and, as a result, the mechanical strength of the joint because of sufficient laser beam energy density level to melt the material more effectively.
- The microstructure of the molten pool is generally composed of solidification of DSS. Depending on the heat conduction coefficient and different temperature gradient, the molten pool microstructure including columnar dendritic and inter-dendritic microstructures at boundary line area of the molten pool with the DSS base metal. At the center of the pool due to the higher heating cycle and lower cooling rate, mainly the cellular microstructure with epitaxial grain growth is observed.
- When the laser power increased from 400 to 450 W, at the region near the fusion line of the DSS the microhardness values increased about 50 HV while at the center of the fusion zone the maximum increase rate reached to the 250 HV.
- Due to the higher temperature gradient at laser power of 450 W, the microhardness values clearly reduced from center of the fusion zone to the AISI 1060 base metal because of formation coarser grain cellular microstructure and more tempered martensitic microstructure.
- According to the numerical simulation results, by increasing the laser power from 250 to 400 W, the extension of high temperature region (more than 1800 °C) raised about 150 percent at both depth and width. Due to the higher thermal conductivity rate of AISI 1060 steel (more than 3 fold), the extension of region with the temperature higher than 300 °C is clearly more than DSS side.
- The high temperature region extended more than AISI 1060 because of lower thermal conductivity coefficient and lower melting point about 100 °C. Therefore, the wider region including heat affected zone and melt pool at upper part of the weld melt pool region and adjacent areas is formed compared to the AISI 1060 steel.
- There was, however, a notable difference at the melt pool width from the upper to the lower part of the melt pool width at the DSS steel side, as compared with the AISI 1060 one, according to the lower thermal conductivity and melting point of DSS steel. The high temperature region was extended more than AISI 1060 because of the lower thermal conductivity coefficient and the lower melting point of about 100 °C. Therefore, the wider region including the heat affected zone and the melt pool at upper part of the weld melt pool region and the adjacent areas was formed, as compared to the AISI 1060 steel.
- The fracture surface of carbon steel side of the joint shows a brittle fracture mechanism due to the martensitic nature of the microstructure of carbon steel while the fracture cross-section of the DSS side of the joint shows a mostly ductile fracture mode compared to carbon steel. The impact of dissimilar laser welding parameters on the resultant microstructural changes, weld geometry, and mechanical characterizations of the dissimilar joint was analyzed by the experimental design. Through adjusting the incident laser power to the workpiece surface, linear movement speed, distance of nozzle from the focal point, and beam deviation for each material, the statistical analysis of the weld joint characterization was conducted.

## CRediT authorship contribution statement

**Mohammad Behzad Botlani Esfahani:** Writing – original draft, Data curation, Conceptualization. **Arash Karimipour:** Writing – original draft, Supervision, Investigation. **Mohammad Akbari:** Writing – original draft, Methodology, Formal analysis. **Ali Abdollahi:** Validation, Software. **Mohammad Najafi:** Writing – original draft, Resources.

## Declaration of competing interest

The authors declare that they have no known competing financial interests or personal relationships that could have appeared to influence the work reported in this paper.

## References


[1] A. Hamada, A. Khosravifard, M. Ali, S. Ghosh, M. Jaskari, M. Hietala, A. Järvenpää, M. Newishy, Micromechanical analysis and finite element modelling of laser-welded 5-mm-thick dissimilar joints between 316L stainless steel and low-alloyed ultra-high-strength steel, Mater. Sci. Eng., A 882 (2023) 145442.

[2] A. Hamada, A. Khosravifard, S. Ghosh, M. Jaskari, M. Kreins, W. Abd-Elaziem, M. Wahba, E. Ahmed, T. Allam, Enhancement of strength in laser-joined Al-TRIP and Si-TRIP steels: microstructural insights and deformation analysis, Mater. Sci. Eng., A 885 (2023) 145591.

[3] A. Hamada, S. Ghosh, M. Ali, M. Jaskari, A. Järvenpää, Studying the strengthening mechanisms and mechanical properties of dissimilar laser-welded butt joints of medium-Mn stainless steel and automotive high-strength carbon steel, Mater. Sci. Eng., A 856 (2022) 143936.

[4] M. Hietala, M. Jaskari, M. Ali, A. Järvenpää, A. Hamada, Dissimilar laser welding of austenitic stainless steel and abrasion-resistant steel: microstructural evolution and mechanical properties enhanced by post-weld heat treatment, Materials 14 (2021) 5580, https://doi.org/10.3390/ma14195580.

[5] Anup Kumar Maurya, Chandan Pandey, Rahul Chhibber, Dissimilar welding of duplex stainless steel with Ni alloys: a review, Int. J. Pres. Ves. Pip. 192 (2021).

[6] R. Gunn, Duplex Stainless Steels: Microstructure, Properties and Applications, 1997.

[7] Ivar Weibull, Duplex stainless steels and their application, particularly in centrifugal separators. Part A History & Development, Mater. Des. 8 (1) (1987) 35–40.

[8] K. Devendranath Ramkumar, D. Mishra, M.K. Vignesh, B. Ganesh Raj, N. Arivazhagan, S.V. Naren, S. Suresh Kumar, Metallurgical and mechanical characterization of electron beam welded super-duplex stainless steel UNS 32750, J. Manuf. Process. 16 (4) (2014) 527–534.

[9] S. Saravanan, K. Raghukandan, N. Sivagurumanikandan, Pulsed Nd: YAG laser welding and subsequent post-weld heat treatment on super duplex stainless steel, J. Manuf. Process. 25 (2017) 284–289.

[10] Y.S. Sato, T.W. Nelson, C.J. Sterling, R.J. Steel, C.-O. Pettersson, Microstructure and mechanical properties of friction stir welded SAF 2507 super duplex stainless steel, Mater. Sci. Eng., A 397 (1–2) (2005) 376–384.

[11] P. Luchtenberg, P.T. de Campos, P. Soares, C.A.H. Laurindo, O. Maranho, R.D. Torres, Effect of welding energy on the corrosion and tribological properties of duplex stainless steel weld overlay deposited by GMAW/CMT process, Surf. Coat. Technol. 375 (2019) 688–693.

[12] Aditya N. Chaudhari, Kartikey Dixit, Gursimer S. Bhatia, Bharat Singh, Piyush Singhal, Kuldeep K. Saxena, Welding behaviour of duplex stainless steel AISI 2205: a review, Mater. Today: Proc. 18 (Part 7) (2019) 2731–2737.

[13] D.S. Pamuji, M.L. Hakim, Sutrisna and Novianto, Investigation of mechanical, microstructure, and corrosion properties of duplex stainless steel joint for natural gas processing facilities, IOP Conf. Ser. Earth Environ. Sci. 1151 (2023) 012056.

[14] A. Pramanik, G. Littlefair, A.K. Basak, Weldability of duplex stainless steel, Mater. Manuf. Process. 30 (9) (2015).

[15] Waris N. Khan, Rahul Chhibber, Experimental investigation on dissimilar weld between super duplex stainless steel 2507 and API X70 pipeline steel, Proc. Inst. Mech. Eng., Part L 235 (8) (2021).

[16] Ceyhun Köse, Ceyhun Topal, Effect of heat input and post-weld heat treatment on surface, texture, microstructure, and mechanical properties of dissimilar laser beam welded AISI 2507 super duplex to AISI 904L super austenitic stainless steels, J. Manuf. Process. 73 (2022) 861–894.

[17] H.S. Abdo, A.H. Seikh, J.A. Mohammed, T. Uzzaman, Ameliorative corrosion resistance and microstructure characterization of 2205 duplex stainless steel by regulating the parameters of pulsed Nd:YAG laser beam welding, Metals 11 (2021) 1206.

[18] S. Saravanan, N. Sivagurumanikandan, K. Raghukandan, Effect of process parameters in microstructural and mechanical properties of Nd: YAG laser welded super duplex stainless steel, Mater. Today: Proc. 39 (Part 4) (2021) 1248–1253.

[19] Alireza Karimi, Arash Karimipour, Mohammad Akbari, Mohammad Mehdi Razzaghi, Mehdi Jamali Ghahderijani, Investigating the mechanical properties and fusion zone microstructure of dissimilar laser weld joint of duplex 2205 stainless steel and A516 carbon steel, Opt Laser. Technol. 158 (2023) 108875.

[20] R. Moradi, et al., Microstructural studies on laser welding of Inconel 718 to 2304 duplex stainless steel with a focus on optimazing process parameters and achieving the Maximum fracture strength, Journal of Advanced Materials in Engineering (Esteghlal) 40 (1) (2022) 45–63.

[21] https://www.steeliranian.com.

[22] P. Sahoo, T. Debroy, M. McNallan, Surface tension of binary metal—surface active solute systems under conditions relevant to welding metallurgy, Metall. Trans. A B 19 (1988) 483–491.

[23] M.J. Kholoud, M. Akbari, Numerical investigation of molten pool dimension, temperature field and melting flow during pulsed laser welding of Ti-6Al-4V alloy sheets with different thicknesses, J. Laser Appl. 33 (3) (2021) 032012, https://doi.org/10.2351/7.0000436.

[24] Y. Ai, P. Jiang, X. Shao, P. Li, C. Wang, A three-dimensional numerical simulation model for weld characteristics analysis in fiber laser keyhole welding, Int. J. Heat Mass Tran. 108 (2017) 614–626.

[25] W. Ke, X. Bu, J. Oliveira, W. Xu, Z. Wang, Z. Zeng, Modeling and numerical study of keyhole-induced porosity formation in laser beam oscillating welding of 5A06 aluminum alloy, Opt Laser. Technol. 133 (2021) 106540.

[26] S. Katayama, Handbook of Laser Welding Technologies, Elsevier, 2013.

[27] P. Coppa, A. Consorti, Normal emissivity of samples surrounded by surfaces at diverse temperatures, Measurement 38 (2) (2005) 124–131.

[28] B. Chang, C. Allen, J. Blackburn, P. Hilton, D. Du, Fluid flow characteristics and porosity behavior in full penetration laser welding of a titanium alloy, Metall. Mater. Trans. B 46 (2015) 906–918.

[29] J.G. Berryman, S.C. Blair, Kozeny–Carman relations and image processing methods for estimating Darcy's constant, J. Appl. Phys. 62 (6) (1987) 2221–2228.

[30] B. Hu, S. Hu, J. Shen, Y. Li, Modeling of keyhole dynamics and analysis of energy absorption efficiency based on Fresnel law during deep-penetration laser spot welding, Comput. Mater. Sci. 97 (2015) 48–54.

[31] Y. Ai, P. Jiang, C. Wang, G. Mi, S. Geng, Experimental and numerical analysis of molten pool and keyhole profile during high-power deep-penetration laser welding, Int. J. Heat Mass Tran. 126 (2018) 779–789.

[32] W.M. Steen, J. Mazumder, Laser Material Processing, 2010 ,.

[33] Köse Ceyhun, Dissimilar laser beam welding of AISI 420 martensitic stainless steel to AISI 2205 duplex stainless steel: effect of post-weld heat treatment on microstructure and mechanical properties, J. Mater. Eng. Perform. 30 (2021) 7417–7448.

[34] A. Hamada, M. Ali, S. Ghosh, M. Jaskari, M. Keskitalo, A. Järvenpää, Mechanical performance and formability of laser-welded dissimilar butt joints between medium-Mn stainless steel and high-strength carbon steel, Mater. Sci. Eng., A 831 (2022) 142200.